Geometry-driven asymmetric cell divisions pattern cell cycles and zygotic genome activation in the zebrafish embryo

Nikhil Mishra, Yuting I. Li, Edouard Hannezo, and Carl-Philipp Heisenberg*
Institute of Science and Technology Austria, Klosterneuburg, Austria
*e-mail: heisenberg@ista.ac.at

Abstract

Embryo geometry is one of the most consistent traits of a species, suggesting that it may serve as a foundational principle for developmental reproducibility and robustness. Here, we show that the zebrafish zygote geometry directs asymmetric cell divisions in the forming blastoderm, establishing radial gradients of cell volume and, consequently, the nucleocytoplasmic ratio. These gradients organize cell divisions along mitotic phase waves, with individual cell periods determined cell-autonomously by the nucleocytoplasmic ratio. Remarkably, we found that this geometry-generated cell volume gradient not only instructs mitotic waves but also spatially patterns zygotic genome activation (ZGA) during the midblastula transition. Thus, our study reveals a novel symmetry-breaking function of early embryo geometry in cell cycle and ZGA patterning, establishing the blueprint for further embryonic development.

Main

Cell cycles in the zebrafish embryo are synchronized in a cell-autonomous manner

Metazoan development begins with a single cell, the zygote, which undergoes several rounds of rapid divisions (cleavages) to generate a large population of cells capable of adopting multiple fates and exhibiting diverse morphogenetic behaviors. In many invertebrate and vertebrate species, these early divisions are initially highly synchronous. This cell cycle synchrony is best understood in *Drosophila*, where it is driven by the propagation of a chemical wave. In cleavage-stage *Drosophila* embryos, which are syncytial, nuclear cycles synchronize through "sweep waves"- a combination of coupling-dependent trigger waves and coupling-independent phase waves of Cyclin-dependent kinase 1 (Cdk1) activity propagating through the cytoplasm[1]. Similar mechanisms have been observed in *Xenopus* egg extracts, another syncytial system, where nuclear divisions are coordinated by trigger waves of Cdk1 activity[2]. By contrast, in intact *Xenopus* embryos, where cells are fully separated, early cleavage divisions synchronize independently of cell-cell coupling[3]. Notably, across systems, the propagation of cell cycle waves slows progressively with successive cleavage rounds, leading to 'metasynchronization', where cell cycles remain spatially patterned before eventually becoming fully desynchronized[1,3,4].

Although conserved across diverse species, the mechanistic basis for cell cycle meta- and desynchronization is only poorly understood. Notably, the loss of cell cycle synchrony often coincides with the midblastula transition (MBT), a stage characterized by zygotic genome activation (ZGA) and the initiation of morphogenetic movements[3,5,6]. This correlation suggests functional links between these processes. Previous studies have proposed that ZGA is triggered by developmental timing and the maturation of cellular components, such as the nuclear pore complex[7]. Additionally, factors like the counting of cell cycles, lengthening of the cell cycle to allow more time for transcription, and the titration of transcriptional repressors - achieved through a reduction in the relative size of the nucleus to the cytoplasm (nucleocytoplasmic ratio) during reductive cell divisions - have been implicated[8–13]. Yet, whether and how these factors are linked to cell cycle synchronization and how ZGA is not only temporally but also spatially regulated within the early embryo, remains unclear.

Initial cleavages in the zebrafish embryo are meroblastic; i.e. the cytoplasm but not the yolk is partitioned through cytokinesis[4]. Cell cycles at this stage occur highly synchronously, to begin with, and gradually desynchronize (metasynchrony) before completely desynchronizing at division round 10[4]. Importantly, while the cleavage-stage cells cycle between only the S and M phases, complete desynchronization at division round 10 is thought to occur mainly due to a heterogeneous introduction of gap phases to the cell cycles[14]. To determine the spatiotemporal pattern of cell divisions in cleavage-stage zebrafish embryos, we recorded time-lapse images of Tg*(actb2:rfp-pcna)* embryos, allowing us to reliably score the onset of mitosis[15]. Consistent with previous reports, we observed three distinct phases with different extents of mitotic synchrony[4,5]. In the first three cell cleavage division rounds, cell cycles exhibited very high synchrony (**synchronous phase**) (Fig. 1B, S1A-B). Thereafter, cell divisions from cleavage rounds four to nine showed slight but clearly detectable delays (**metasynchronous phase**) (Fig. 1B, S1A-B). These delays increased throughout the metasynchronous phase, with cells in division round four dividing with a mean division timing

variance of 0.10 min^2 and in division round 9 with 3.43 min^2 (Fig. 1B). Notably, as previously reported, these metasynchronous divisions occurred in a spatiotemporally patterned manner, forming a radial 'mitotic wave' that originates near the animal pole (AP), where cells divide first, and propagates toward the margin, where they divide last (Fig. 1C, S1C-D)[4,16,17]. Furthermore, consistent with the increasing variance in division timings during the metasynchronous phase, the speed at which this mitotic wave travels gradually decreased over consecutive division rounds (Fig. 1D). After round nine, cells divided largely non-synchronously, marking the onset of the **asynchronous phase**.

To understand how cell cycles are seemingly coordinated into radial mitotic waves during the metasynchronous phase, we asked whether neighboring cells within the embryo can synchronize their cell division cycles. We found that neighboring cells that originated from a common cell division (sister cells) were significantly more synchronized than those not originating from the same cell division (non-sister cells) (Fig. 1E). This suggests that cell lineage, rather than cell-cell proximity, affects cell division timing such that cells closely related by lineage likely inherit more synchronized internal 'clocks' than those inherited by unrelated cells. To further challenge this possibility, we artificially desynchronized cell cycles at the 32/64-cell stage through mosaic Histone 1 protein injections, previously been shown to effectively alter cell cycle progression[18–20]. We found that Histone 1-positive and thus desynchronized cells failed to resynchronize with their neighboring control cells by division round 9, after which cell cycles normally desynchronize in control embryos (Fig. 1F, S2, Movie S2). To address the possibility that these cell cycles could have resynchronized given sufficient time, we assessed cell cycle progression in embryos ectopically expressing the Cdk1 inhibitor, Chek1, through *chek1* mRNA injection in the one-celled embryo, which, by being heterogeneously distributed in the embryo, has previously been shown to interfere with cell cycle synchronization[21]. Chek1-overexpressing embryos exhibited cell cycle desynchronization significantly earlier than control embryos, and failed to resynchronize despite completing all cleavage division rounds (Fig. 1G, S2, Movie S3). These observations suggest that cell-cell coupling through mechanisms other than cell lineage plays only a minor role, if any, in cell cycle synchronization in the zebrafish embryo.

The transition from synchrony to metasynchrony was gradual rather than abrupt, suggesting a progressive accumulation of delays rather than distinct switches leading to the observed loss of synchrony (Fig. 1B). Importantly, this gradual loss of synchrony was due to unequal cell cycle periods. For instance, between the metasynchronous division rounds 6-8, cells at the margin cycled with 2-4% longer periods than those at the AP. This discrepancy arose exclusively due to a longer S-phase, which increased in cells as a function of their distance from the animal pole (Fig. 1H-I). Such period gradients might lead to the observed gradual slowing down of the radial mitotic wave by accumulating increasing delays in the marginal cells over consecutive division rounds. To test this hypothesis, we assumed that the period, T, is a linear function of the distance 'z' from the AP where $T = T_0(1 + \frac{kz}{L})$, with T_0 being the typical period at the AP, L the total AP-margin distance, and k a dimensionless constant of proportionality. This implies that the speed of the mitotic wave, v, in the nth division round is expected to be inversely proportional to n (Fig. 1D) with $v = \frac{L}{T_0}\frac{1}{kn}$. To compare our experimental observations with these theoretical predictions, we first performed linear regression on the division timings to obtain the wave speed for each division round (Fig. S1D). We

then fitted the obtained *v* against $\frac{1}{n}$ using the least square fit. Using *k=1.9%,* we obtained a close match between experiments and theory (Fig. 1D), suggesting that a 1.9% slower cell cycle at the margin would, in principle, be sufficient to explain the observed slowing down of the mitotic waves during consecutive division rounds. Considering that we experimentally observed a 2-4% longer period at the margin, close to the theoretically predicted 1.9%, this suggests that a linear gradient of cell cycle periods, rather than cell-cell coupling, gives rise to the observed radial mitotic waves found during embryonic cleavages.

Increased cell-cell coupling reshapes the mitotic wave and prevents desynchronization

Next, to verify our conclusion that the mitotic waves are produced in a coupling-independent manner, we asked how they would appear if the cell cycles were instead coupled. To that end, we performed numerical simulations of the Kuramoto model of interacting oscillators on a hemisphere with free boundary conditions[22] (Fig. 2A). The oscillators were placed on a Fibonacci lattice covering the hemisphere, with nearest neighbors obtained with Delaunay triangulation. The phases of the oscillators obeyed the following equation: $\delta_t\theta_i = \omega_i + \epsilon \sum_{j\in N_i} sin(\theta_j - \theta_i)$ where ω_i represents the natural frequency of the *i*-th oscillator, and the second term describes the interactions between neighboring oscillators parametrized by the interaction strength ϵ, with N_i being the nearest neighbors of the *i*-th oscillator. Due to cell-to-cell variations, we further assumed the presence of noise in the cell cycle lengths. Mathematically, we decomposed the frequencies into two parts $\omega_i = \varpi(z) + \Lambda_i$, where the first term $\varpi(z)$, is the inherent AP-to-margin oscillation gradient, and the second term is an independent spatial noise with covariance $\langle \Lambda_i \Lambda_j \rangle = \sigma\delta_{ij}$. Simulations with small interaction strength (ϵ) and low noise (σ) recapitulated the wild-type behavior, where mitotic waves originated at the AP, and accumulated delays causing a gradual slow-down over time (Fig. 2B-C). In contrast, the introduction of greater interaction strength and noise led the system to self-organize into smooth mitotic waves originating at the margin, similar to the case in *Xenopus* egg extracts, even though the 'natural' cell cycle lengths at the AP were preset to be shorter on average[23] (Fig. 2B, D). For even larger values of noise, multiple waves emerged from random points of the simulated embryo (Fig. 2B). Overall, this theoretical phase diagram suggests that wild-type embryos are characterized by low to intermediate noise and very little coupling and that increasing cell coupling should, in theory, shift the origin of the mitotic wave from the AP to the blastoderm margin.

To experimentally test this prediction, we syncytialized cleavage-stage embryos by preventing cytokinesis but not karyokinesis through transient Aurora Kinase B inactivation[24] (Fig. 2E-F). We reasoned that a syncytialized embryo would mimic the situation in *Drosophila* embryos and *Xenopus* egg extracts, both syncytial systems, where cell cycles are synchronized partially or completely through coupling-dependent trigger waves and would, therefore, comprise a coupled system. Remarkably, we found, consistent with our theoretical predictions, that in syncytial embryos, the mitotic wave originated at the margin rather than at the AP, as it does in control embryos (Fig. 2B, D, F Movies S1, S4). Comparing the wave characteristic at the 8th round of divisions allowed us to estimate the effective coupling to noise ratio in syncytial embryos (Fig. 2G). Interestingly, when examining not just the overall origin of the waves but also the quantitative changes in synchronization over time (quantified by division time variance for different division rounds) predicted another key difference in the model between intact and syncytial embryos. Indeed, in the

absence of coupling (intact embryo), noise should gradually accumulate, leading to monotonously increasing timing variance, whereas, with coupling (syncytial embryo), the variance should plateau over time with a characteristic time scale dependent on the exact value of the coupling parameter (Fig. 2H). Strikingly, this was confirmed in our experiments: in syncytial embryos (unlike in controls), 'cells' continued to cycle metasynchronously even beyond the 10th division round, indicating tight coupling between cell cycles (Fig. S3A, Movies S1, S4), with the evolution of the variance well-described by our theoretical prediction (for ϵ=0.08 and σ=0.028 Fig. 2H). For intact embryos, the variance continuously increases, although with an even faster temporal scaling than in the model for later cleavages (Fig. 2I). Interestingly, considering the fact that cytokinesis is incomplete at early cleavages (i.e. that couplings initially exist but rapidly decay to near zero for later cleavages) could explain quantitatively the experimental data for intact embryos (see SI Theory Note for more details on the approach and assumptions)[25].

Finally, to further challenge the increased coupling of syncytial 'cells', we injected *chek1* mRNA into embryos before syncytialization and assessed whether they could resist premature desynchronization typically caused *by chek1* expression in intact wild-type embryos (Figs. 1G, S1, Movie S3). Indeed, we reasoned theoretically that the values of couplings inferred for syncytial embryos were large enough that they should be able to override a significant increase in noise, such as the desynchronizing effects of *chek1* expression (Fig. 2B). Indeed, we found that in *chek1*-expressing embryos, the mitotic waves originated at the margin, and 'cells' continued to cycle metasynchronously even beyond the 10th division round, suggesting that cells in the syncytial embryo are, in fact, tightly coupled. (Fig. S3B-C, Movie S5). By extension, this implies that such a coupling is absent/minimal in intact embryos and, consequently, that mitotic waves are produced largely independently of cell-cell interactions in wild-type embryos. Collectively, these findings suggest that cell cycles are only weakly coupled during cleavages and that metasynchrony arises predominantly by cell-autonomous processes.

Early embryo geometry establishes a cell volume gradient along the AP-margin axis through guided asymmetric cell divisions

For the cell cycle to slow down from the AP to the margin in a predominantly cell-autonomous manner, there must be a factor causing unequal lengthening of the S-phase along the AP-margin axis. Among the most important factors regulating S-phase length is the nucleocytoplasmic (N/C) ratio[26,27]. A high N/C ratio causes S-phase lengthening, for instance, by retarding Cdk1 activation[26]. Consistent with such an effect of the N/C ratio on cell cycle length, we found that the length of the S-phase across the metasynchronous cleavage rounds negatively correlated with cell volume (Fig. S4A-B). Therefore, we hypothesized that an AP-margin gradient of cell volumes in the cleavage-stage embryo might be responsible for unequally slowing down the cell cycle length from the AP to the margin. To test this hypothesis, we measured cell volumes by semi-automatically segmenting surface cells at the 128-cell stage (round 8). Indeed, we found that, on average, cells closer to the AP were significantly larger than those away from it (Figs. 3A, S4G). To determine at what stage such a volume gradient first becomes apparent, we also measured cell volumes in embryos at the 8-cell stage (round 4) and the 16-cell stage (round 5) - the first stages where cells can be classified as being 'central' or 'peripheral' based on their position. Interestingly, we observed that cells closer to the AP were consistently larger than the marginal cells at both these stages, showing that the AP-

margin gradient of cell volumes arises already in the very early embryo (Fig. 3B, C). However, no such gradient was observed for the nuclear volume, indicating that the peripheral cells have a larger N/C ratio (Fig. 3B). Furthermore, the cell volume gradient not only persisted but was also further enhanced by subsequent cell divisions, as mother cells having unequal sizes themselves again divided asymmetrically to produce yet unequally sized daughters, thereby further diversifying cell volumes through cell lineage in addition to the already established position-driven cell volume diversity (Fig. 3D). For such unequal cell divisions to robustly give rise to a gradient in cell volumes along the AP-margin axis, upon division the daughter cell closer to the AP must be on average bigger than the daughter cell further from the AP. In line with this, we found that cell divisions in the early cleavage stages showed a tendency to produce larger daughter cells closer to AP, with the central daughter cell (closer to AP) being, on average, ~12.4% larger by volume than its peripheral sister cell (away from AP) (Fig. 3E).

To determine what causes such patterned asymmetric cell divisions, we investigated how cell divisions are oriented and the cleavage plane positioned in the early embryo. While several sophisticated models have been proposed to explain the orientation and positioning of the cleavage plane across systems, we started by first testing if following the simplest model, the ~140-year old Hertwig's rule, can recapitulate the experimentally observed pattern of asymmetry[28,29]. More specifically, we assumed that the mitotic spindle in dividing blastomeres would orient along the longest cell axis, thereby dividing the cell along this axis. To test if such a geometry-driven mechanism would suffice to generate the observed pattern of asymmetric cell divisions and, therefore, the cell volume gradient, we predicted daughter cell volumes at the 16-cell stage by first identifying the longest axes of segmented cells at the 8-cell stage through Principal Component Analysis and then bisecting them to obtain two daughter cells from each division[30] (Fig. 3E). Indeed, we found that with this approach, the predicted daughter cell size asymmetry closely matched the observed asymmetry for most cell divisions, such that the central daughter cells (closer to the AP) at the 16-cell stage were, on average, ~18.5% larger than their peripheral sister cells (further away from the AP) by volume (Fig. 3E). Importantly, this tendency of central daughter cells being bigger than peripheral ones is determined by the specific geometry of the first cell of the fertilized egg, the blastodisc, that is delineated not only by a plasma membrane at its outer side, but also by the interface to the yolk granules on its inner side[4,31]. As the interface to the yolk granules is curved, the first cell division will give rise to equally sized daughter cells that are more pointed and narrow at their peripheral ends. Dividing these cells again along the same axis will then, as a result, generate daughter cells where the central cell is larger than the peripheral one. This suggests that a gradient of cell volumes along the AP-margin axis in the cleaving embryo can be explained by the specific geometry of the first cell in the fertilized egg leading to unequal cell division along the AP-margin axis during subsequent division rounds.

Cell volume gradient causes patterned cell cycle lengthening along the AP-margin axis

Whereas the influence of cell volume on cell cycle length is established in several systems, such a relationship in zebrafish embryos is still unclear, owing to contradicting reports as to the determinative role of cell size in this context[5,17]. Therefore, to unequivocally establish the role of cell volume, and consequently the N/C ratio, in determining cell cycle lengths, we first increased the N/C ratio at the one-cell stage by aspirating cytoplasm from the blastodisc (Fig. S4C). Consistent with

229 the role of high N/C ratios in prolonging cell cycles, we observed that in different embryos, the S-
230 phase lengthened prematurely or significantly more, and cell cycles desynchronized earlier than in
231 control embryos (Fig. S4D). Reversely, we decreased the N/C ratio by replicating an experiment by
232 Kane and Kimmel[4], where we aspirated one nucleus from two (or four)-cell stage embryos (Fig.
233 S4E). In such embryos, only the control half initially underwent cleavages, while no cleavages
234 occurred in the other, enucleated half (Fig. S4E, Movie S6). However, in a subset of the embryos at
235 the 4th or 5th division round, nuclei from the control half invaded the enucleated half, which then
236 commenced cleavages (Fig. S4E, Movie S6). Notably, despite all nuclei at this stage having
237 undergone the same number of cycles, those in the previously enucleated half now resided in a
238 much larger volume of cytoplasm and, consequently, displayed a smaller N/C ratio. In line with
239 previous findings, these nuclei displayed delayed S-phase lengthening and continued to cycle
240 metasynchronously beyond the 10th division round, the stage when cell cycles in the 'control' half
241 typically desynchronize[5] (Fig. S4F).

242 Having confirmed that the N/C ratio, in principle, can influence the S-phase length, we asked how
243 perturbing the embryo-scale cell volume gradient within the cleaving embryo would affect cell cycle
244 (meta)synchrony and, consequently, the mitotic wave. To alter the cell volume gradient, we first
245 generated bi-lobed embryos displaying two ectopic 'animal poles' by mounting two-cell stage
246 embryos in low melting point agarose (0.67% w/v in E3 buffer) when the first cytokinesis was in
247 progress (Fig. 4A). We reasoned that spatially confining and, therefore, reshaping the embryo in this
248 manner would produce larger cells away from the AP at the two ectopic (morphological) animal
249 poles. Interestingly, we found that not only the gradient of cell volumes was reshaped in the embryo,
250 but also that two mitotic waves, one from each of the two ectopic APs, supporting the notion that the
251 cell volume gradient is linked to the emergence of the mitotic wave (Fig. 4A, B, Movie S7). To further
252 challenge this suggestion, we removed a part of the yolk on the vegetal side of the two-cell stage
253 embryo to increase the curvature of the blastodisc (the two blastomeres positioned on the yolk cell;
254 Fig. 4C). Based on our analysis indicating that the cell volume gradient is a product of the curvature
255 of the blastodisc-yolk interface, we reasoned that this increased curvature would reorient the longest
256 axes of the two cells, such that they align more along the animal-vegetal (AV) axis, which would
257 then amplify the volume asymmetry of cleavage divisions and, consequently, the phase difference
258 between cell cycles (Fig. 4C). Strikingly, we found that in yolk-severed embryos with cell divisions
259 more aligned along the AV axis, the mitotic wave indeed showed a greater cell division timing
260 variance compared to the control embryos (Fig. 4C-D, Movie S8). Taken together, these
261 observations strongly support the notion that a gradient of cell volume along the AP-margin axis,
262 guided by embryo geometry, causes the generation of a gradient of S-phase lengths along the AP-
263 margin axis of the blastoderm, thereby generating radial mitotic waves in the zebrafish embryo.

264 Among the major responders to a high N/C ratio is Chek1, which, when active, delays the S-M
265 transition[26]. Therefore, having determined that a gradient of cell volumes patterns cell cycle lengths
266 in the zebrafish embryo, we inquired whether Chek1 mediates the effect of cell volume on S-phase
267 length. To that end, we inhibited Chek1 activity by treating embryos with 10 μM PF477736, a specific
268 Chek1 activity inhibitor[32]. If Chek1 activity is required for the gradual metasynchronization of cell
269 cycles through unequal S-phase lengthening, the cell cycle progression would be expected to show
270 less variations in the treated embryos. Consistent with this, we found that, while Chek1-inhibited
271 embryos produced mitotic waves like those in control embryos, they indeed exhibited a lower mitotic

division timing variance (Fig. 4E, Movie S9). This suggests that Chek1 activity is critical for translating a cell volume gradient into a mitotic wave along the AP-margin axis of the blastoderm.

Cell volume/cell cycle period gradients pattern ZGA along the AP-margin axis

Finally, we asked if the geometry-driven cell volume gradient and the resulting patterned mitotic metasynchrony play a developmental role that may impact embryogenesis beyond the cleavage stages. Mitotic metasynchrony in zebrafish embryos diminishes concomitantly with the onset of ZGA, which sets up the blueprint for cell fate heterogeneity, a process central to metazoan development[5]. Therefore, considering the previously reported roles of cell volume and cell cycle length on ZGA, we asked if the onset of zygotic transcription is influenced by the observed cell volume gradient and resulting mitotic metasynchrony[10]. To this end, we assessed when and where zygotic transcription is initiated in the embryo by performing native pri-*miR430* transcription imaging through MOrpholino VIsualisation of Expression (MOVIE)[33] (Fig. 5A). *miR430* genes are among the first and most transcribed genes in fish, and hence, an excellent candidate to assess zygotic transcription onset[34,35]. In most embryos, we observed the first instances of *miR430* transcription in division round 9. Interestingly, we found that the expression was initiated in a graded manner during division rounds 9 and 10, first appearing in cells close to the margin, followed by cells in the intermediate zone between the margin and AP, and last in cells at the AP (Figs. 5B, S5, Movie S10). This suggests that zygotic transcription onset occurs as a spatiotemporal gradient along the AP-margin axis (Figs. 5B, S5). To determine whether this zygotic transcription onset pattern arises due to the gradient of cell volume and/or cell cycle length along this axis, we examined bi-lobed embryos, where both gradients are perturbed (Figs. 4A-B, 5C). Importantly, unlike in control embryos, cells at the AP in bi-lobed embryos are smaller and cycle slower than those in the intermediate zone (Figs. 4A-B). Analysis of these bi-lobed embryos showed that, in contrast to control embryos, *miR430* transcription was first initiated at the embryonic margin and the AP, where cells were smallest in these embryos before it did in the intermediate zone (Fig. 5D, Movie S11). This suggests that the gradient of cell volume and/or cell cycle length along the AP-margin axis influences the onset of zygotic transcription along this axis, thereby spatiotemporally linking early embryo geometry to the onset of zygotic gene expression.

Discussion

Previous research has shown that the shape of the zebrafish egg - particularly the blastodisc, from which all cells and tissues of the embryo originate - is determined by ooplasmic streaming, which segregates yolk granules from the cytoplasm within the fertilized egg[31]. Our data now suggest that if the mitotic spindle consistently aligns with the longest cell axis, as described by Hertwig's rule, this alone can explain how the initial shape of the blastodisc leads to unequal cell divisions during successive reductive cleavages. This process ultimately generates a gradient of cell volumes along the AP-margin axis of the developing blastoderm, which in turn influences cell cycle progression and ZGA along this axis. While this does not exclude the possibility that more complex mechanisms - such as differential interactions between spindle microtubules and yolk granules versus the cellular cortex or plasma membrane - may also contribute to asymmetric cell division, our findings suggest that such complexities are not necessary to explain the observed

313 outcomes. Therefore, the formation of a cell volume gradient, and consequently the regulation of
314 the cell cycle and ZGA patterns, is a direct consequence of the blastodisc's shape.
315
316 We have previously demonstrated that radially patterned cell behavior and asymmetric tissue
317 compaction along the AP-margin axis of the blastoderm occur at the onset of gastrulation, serving
318 as essential conditions for proper gastrulation[6,21]. It is plausible that these differences in tissue
319 properties arise from distinct transcription profiles and dynamics driven by the differential ZGA
320 patterns reported in this study. Thus, our findings likely connect two key developmental milestones:
321 blastodisc shape determination immediately after fertilization and asymmetric tissue fluidization at
322 the onset of gastrulation. This suggests that inherent geometric asymmetries in the blastodisc shape
323 manifest much later, as their effects amplify over time during the first proliferative phase of
324 embryogenesis - resolving an important missing link in early vertebrate development.

325 Furthermore, our work provides evidence that the cell volume gradient influences the cell cycle
326 length gradient by establishing a gradient in the nucleocytoplasmic (N/C) ratio, which has been
327 previously implicated in controlling cell cycle length[10]. Various mechanisms have been proposed for
328 how the N/C ratio regulates cell cycle length, primarily focusing on its impact on the availability and
329 activity of cell cycle regulators[8,9,11,12]. While our findings support the role of the N/C ratio in
330 determining cell cycle length and that of the cell cycle regulator Chek1 therein, they do not pinpoint
331 a specific underlying mechanism. Notably, although our observations align with the idea that cell
332 volume regulation is the primary mechanism for cell cycle synchronization in the embryo, additional
333 factors may also modulate this process. For instance, synchronization during early cleavage stages
334 might be facilitated by cytoplasmic bridges connecting cells at early cleavage stages, allowing mitotic
335 trigger waves to propagate through these connections and synchronize cell cycles. Such transient
336 coupling of cells at early, but not later, cleavage stages is consistent with our mathematical
337 simulations, which suggest that the observed evolution of mitotic timing variance in wild-type
338 embryos is best described by an exponential decay in coupling strength across successive division
339 rounds.

340 Finally, there are multiple potential mechanisms linking the cell volume and/or cell cycle gradients
341 to the onset of zygotic gene transcription. These mechanisms typically propose that either cell
342 volume, and thus the N/C ratio, promotes transcription by the DNA titrating transcriptional
343 repressors, or that a short cell cycle length inhibits transcription by causing competition between the
344 DNA replication and transcription machineries[8–12]. Consistent with this, recent observations in
345 *Xenopus* suggest that ZGA is activated first in the smaller cells at the AP[13]. Our observation that the
346 smaller, slower-cycling cells at the blastoderm margin not only initiate zygotic transcription before
347 the larger, faster-cycling cells at the animal pole but also continue transcription for a longer duration
348 supports the idea that cell cycle length determines the spatiotemporal pattern of zygotic gene
349 transcription. This finding is significant, as it suggests that the regulation of cell cycle synchronization
350 by the cell volume gradient is crucial for its influence on the patterning of zygotic genome activation.

351 Robust regulation of Zygotic Genome Activation (ZGA) is essential for accurate cell fate specification
352 and associated morphogenetic processes. Given its importance, one would assume that the factors
353 regulating ZGA must also be robust themselves. Considering that embryo shape is one of the most
354 distinct and invariant features of animal development, it is plausible that it serves as a major

355 determinant of ZGA and its regulated processes. Several observations support this notion. For
356 instance, in zebrafish embryos, smaller and slower-cycling cells near the margin initiate zygotic
357 transcription first and subsequently adopt the mesendodermal fate, suggesting that early zygotic
358 gene activation may facilitate this process. Similar observations were also made in sea urchins and
359 nematodes, with smaller cells at the vegetal pole of sea urchin embryos cycling slower than larger
360 cells and later assuming a mesodermal fate, and lineages producing cells in *C. elegans* embryos
361 that involute during gastrulation also exhibiting slower cell cycles compared to non-involuting cells[36–
362 38]. Collectively, these previous findings underscore the physiological significance of our observation
363 that the spatiotemporal patterning of ZGA is the product of embryo shape determining the
364 distribution of cell volumes and cell cycle lengths within the early embryo. The specific
365 developmental consequences of this fundamental relationship will likely differ between different
366 species and need to be explored in the specific organismal context.

367

368 # Methods

369 ## Cell cycle analysis

370 Tg(*actb2:rfp-pcna*) embryos were dechorionated and, at the desired stage, mounted in 0.5%
371 agarose gels prepared in E3 buffer with the animal pole facing upward in casts made with 2%
372 agarose solution in E3 buffer[15]. RFP fluorescence was imaged at 23.5 °C using a 20x water-dipping
373 objective on Zeiss LSM800 (N.A.=0.8), LSM880 (N.A.=1.0), or LSM900 (N.A.=1.0) upright confocal
374 microscopes. 200-350 µm-thick Z-stacks were acquired for different experiments with temporal
375 resolutions ranging between 17-65 sec/Z-stack. The presence or absence of nuclear RFP-PCNA
376 fluorescence was used to determine if a cell was in the S or M phase of the cell cycle, respectively[39–
377 41]. The nuclear signal was segmented in Fiji using the Labkit plugin[42,43]. The segmented objects
378 were imported into Bitplane Imaris (https://imaris.oxinst.com/) to generate tracks and obtain
379 tracking-related data, including track start time (S-phase entry), track end time (M-phase entry),
380 track duration (S-phase length), and the nuclear coordinates at the last S-phase time point (position).
381 These data were then analyzed using the Pandas Python library to calculate, for instance, the
382 division timing variance in a given division round, followed by plotting using mainly the Matplotlib
383 and Seaborn libraries[44–46]. Anaphase onset timings for comparison between sister and non-sister
384 cells were determined by generating 3D image stacks of wild-type AB embryos injected with 0.5 pg
385 Histone 1-Alexa Fluor 488 (Catalog #H13188, Invitrogen) at the one-cell stage as described above.

386 ## Mitotic wave speed

387 The mitotic wave speed for a given round of division was determined by first identifying the position
388 of the wave origin and the timing of the wave origination, measuring all other nuclear distances and
389 mitotic entry timings relative to this position and time, and then generating the best fitting distance-
390 time linear curve. In the cases where more than one nucleus could be considered the origin of the
391 mitotic wave due to a simultaneous entry into mitosis, the mean of the 3D coordinates of such nuclei
392 was considered the position of the wave origin.

393 ## Microinjections

394 To visualize cell cycle progression using Histone 1 as the marker, 0.5 pg Histone 1-Alexa Fluor 488
395 was injected at the one-cell stage into wild-type AB or Tg(*actb2:lyn-tdTomato*) embryos[47]. Mosaic

396 perturbation of the cycling period of a subset of the cells was carried out by mounting 32/64-cell
397 stage embryos in 2% agarose solution in E3 buffer and injecting 0.2-0.3 pg of Histone 1-Alexa Fluor
398 488 into such cells. *chek1* overexpression was achieved by injecting 12 pg *chek1* mRNA into the
399 one-cell embryo[13,41]. mRNA was prepared as described previously[21].

400 **Drug treatments**

401 Aurkb function was inhibited by transiently incubating dechorionated <5 min post fertilization (mpf)
402 embryos in 50 μM AZD1152 (Catalog #SML0268, Sigma-Aldrich) solution for 15 min, after which
403 they were returned to E3 buffer. Embryos showing successful nuclear cycling despite a failure of
404 cytokinesis were then imaged as described above. Inhibition of Aurkb function concomitantly with
405 *chek1* overexpression or Histone 1-Alexa Fluor 488 visualization was performed by injecting 12 pg
406 *chek1* mRNA or 0.5 pg Histone 1-Alexa Fluor 488, respectively, at the one-cell stage as described
407 above, followed by incubation in the Aurkb inhibitor. Chek1 activity inhibition was performed by
408 dechorionating <10 mpf embryos and incubating them in 10 μM PF477736 (Catalog #HY-10032,
409 MedChem Express) solution in E3 buffer throughout the duration of analysis.

410 **Nuclear volume measurement**

411 Nuclear RFP-PCNA fluorescence was segmented from Z-stacks by thresholding using Fiji, and their
412 volumes were measured using the 3D Objects Counter plugin[48].

413 **Cell volume measurement**

414 Cell volumes at the 8- and 16-cell stages were measured by semi-automatically generating cell
415 segmentation using the 'Contour' function for surface creation in Bitplane Imaris from Z-stacks of
416 Tg(*actb2:mCherry-CAAX*) embryos[49]. Once segmented, the physical attributes of individual cells,
417 such as volume and position, were exported from Bitplane Imaris as CSV files. The last time point
418 before the onset of the fourth or fifth mitotic round was used to measure the cell volume for the 8-
419 or the 16-cell stage, respectively. Cell volumes at the 128-cell stage were measured by generating
420 cell segmentations using the Limeseg plugin in Fiji and exporting the cell volume data for individual
421 segmented objects[50]. All downstream data analysis was performed in Python, mainly using the
422 Pandas library, and the plots were produced using the Matplotlib and Seaborn libraries.

423 **Daughter cell volume prediction**

424 Cell surfaces generated in Bitplane Imaris at the 8-cell stage were exported as WRL files, imported
425 into MeshLab (https://www.meshlab.net/), from where individual cell surfaces were exported as PLY
426 files. These files were subsequently processed in Python to identify the longest cell axis by
427 performing Principal Component Analysis (PCA), along which the cell was bisected into two
428 daughter cells representing cells at the 16-cell stage[30].

429 **Nearest neighbor distance calculation**

430 Nuclei positions were obtained from Bitplane Imaris, as detailed above. For each nucleus, the three
431 nearest neighbors were identified, and their mean distance from the reference nucleus was
432 calculated using the Pandas library in Python.

433 ## Cytoplasm aspiration

434 Approximately 30 mpf Tg(*actb2:rfp-pcna*) embryos were mounted in E3 buffer on a substrate
435 prepared with 2% agarose solution in E3 buffer. A 20 µm blunt-end needle attached to a 10 µl
436 Hamilton syringe was inserted through the yolk into the blastodisc, and the cytoplasm was carefully
437 aspirated. The nuclear RFP-PCNA signal was constantly observed using a Leica stereo-
438 fluorescence microscope to ensure the nucleus was not extracted together with the cytoplasm.

439 ## Nucleus aspiration

440 The setup and mounting procedure for the nucleus aspiration were the same as for cytoplasm
441 aspiration described above, except that, in this case, the nucleus was aspirated rather than the
442 cytoplasm and from embryos at the two-cell stage rather than the one-cell stage. Care was exercised
443 to ensure that the nucleus was extracted with a negligible volume of the cytoplasm being aspirated
444 in the process.

445 ## Generation of bi-lobed embryos

446 Bi-lobed embryos were created by spatially confining dechorionated embryos at the two-cell stage,
447 still undergoing cytokinesis from the first division round, in 0.5-0.6% agarose in E3 buffer.
448 Microscopy was performed as described above.

449 ## Yolk severing

450 To sever the yolk, dechorionated embryos at the two-cell stage were placed on a substrate of 3%
451 methylcellulose in E3 buffer in a glass dish. Using an eyelash attached to the end of a Pasteur
452 pipette, the vegetal half of the yolk was first punctured to prevent the embryo from exploding due
453 to a buildup of internal pressure during the severing procedure and then carefully sliced. The
454 embryo was allowed to recover for at least 15 minutes after the procedure, followed by mounting
455 and microscopy, as detailed above.

456 ## Cell division angle measurement

457 Four orthogonal sections, each showing four nuclei along the 4th round division plane at the 16-
458 cell stage, were generated using the Fiji Reslice function from Z-stacks of individual Tg(*actb2:rfp-*
459 *pcna*) embryos. The angles between nuclei were then measured using Fiji, as represented in Fig.
460 4D, to obtain the angle of cell divisions in the 4th division round.
461

462 ## miR430 transcription analysis

463 pri-*miR430* transcripts were labelled as described previously[14]. Tg(*actb2:rfp-pcna*) embryos injected
464 with MO1-3-Fluorescein (Gene Tools) at the one-cell stage were mounted in 0.5% agarose solution
465 in E3 buffer in #3 Fluorinated ethylene propylene (FEP) tubes, and Z-stacks were generated with a
466 temporal resolution of approximately one min/Z-stack using a 20x/N.A. 1.33 objective on a Zeiss
467 Lightsheet 7 microscope. Maximum intensity projections of these time-lapse recordings were then
468 used to assess the transcription status of individual nuclei.
469

Acknowledgments

We thank Nicoletta Petridou (EMBL) for sharing results prior to publication. NM was supported by funding from the European Union's Horizon 2020 programme under the Marie Skłodowska-Curie COFUND Actions ISTplus, Grant Agreement No. 754411. YIL acknowledges funding from the European Union's Horizon 2020 research and innovation programme under the Marie Skłodowska-Curie Grant Agreement No. 101034413. The research was supported by funding to C-PH from the NOMIS Foundation, Project ID 1.844. The authors would like to thank past and present members of the Heisenberg and Hannezo groups for discussions, and, in particular, Shayan Shamipour, Viraj Doddihal, Michaela Jovic, Naoya Hino, Feyza Nur Arslan, Roksolana Kobylinska, and Carolina Camelo for feedback on the manuscript draft. This research was supported by the Scientific Service Units (SSU) of ISTA through resources provided by the Aquatics Facility, Imaging & Optics Facility (IOF), Scientific Computing (SciComp) facility, and Lab Support Facility (LSF).

Author Contributions

NM and CPH conceptualized the study. All authors contributed to the design of the experiments. NM (experiments) and YIL (theory) acquired and analyzed the data. All authors contributed to manuscript preparation.

489 ## References

490 1. Deneke, V. E., Melbinger, A., Vergassola, M. & Di Talia, S. Waves of Cdk1 Activity in S Phase
491 Synchronize the Cell Cycle in Drosophila Embryos. *Dev. Cell* **38**, 399–412 (2016).
492 2. Chang, J. B. & Ferrell, J. E. Mitotic trigger waves and the spatial coordination of the Xenopus
493 cell cycle. *Nature* **500**, 603–607 (2013).
494 3. Anderson, G. A., Gelens, L., Baker, J. C. & Ferrell, J. E. Desynchronizing Embryonic Cell
495 Division Waves Reveals the Robustness of Xenopus laevis Development. *Cell Rep.* **21**, 37–46
496 (2017).
497 4. Kimmel, C. B., Ballard, W. W., Kimmel, S. R., Ullmann, B. & Schilling, T. F. Stages of embryonic
498 development of the zebrafish. *Dev. Dyn.* **203**, 253–310 (1995).
499 5. Kane, D. A. & Kimmel, C. B. The zebrafish midblastula transition. *Dev. Camb. Engl.* **119**, 447–
500 456 (1993).
501 6. Petridou, N. I., Grigolon, S., Salbreux, G., Hannezo, E. & Heisenberg, C.-P. Fluidization-
502 mediated tissue spreading by mitotic cell rounding and non-canonical Wnt signalling. *Nat. Cell*
503 *Biol.* **21**, 169–178 (2019).
504 7. Shen, W. *et al.* Comprehensive maturity of nuclear pore complexes regulates zygotic genome
505 activation. *Cell* **185**, 4954-4970.e20 (2022).
506 8. Newport, J. & Kirschner, M. A major developmental transition in early Xenopus embryos: I.
507 characterization and timing of cellular changes at the midblastula stage. *Cell* **30**, 675–686
508 (1982).
509 9. Newport, J. & Kirschner, M. A major developmental transition in early xenopus embryos: II.
510 control of the onset of transcription. *Cell* **30**, 687–696 (1982).
511 10. Langley, A. R., Smith, J. C., Stemple, D. L. & Harvey, S. A. New insights into the maternal
512 to zygotic transition. *Development* **141**, 3834–3841 (2014).
513 11. Edgar, B. A. & Schubiger, G. Parameters controlling transcriptional activation during early
514 drosophila development. *Cell* **44**, 871–877 (1986).

515 12. Kimelman, D., Kirschner, M. & Scherson, T. The events of the midblastula transition in
516 Xenopus are regulated by changes in the cell cycle. *Cell* **48**, 399–407 (1987).
517 13. Chen, H., Einstein, L. C., Little, S. C. & Good, M. C. Spatiotemporal Patterning of Zygotic
518 Genome Activation in a Model Vertebrate Embryo. *Dev. Cell* **49**, 852-866.e7 (2019).
519 14. Zamir, E., Kam, Z. & Yarden, A. Transcription-Dependent Induction of G1 Phase during the
520 Zebra Fish Midblastula Transition. *Mol. Cell. Biol.* **17**, 529–536 (1997).
521 15. Boothe, T. *et al.* A tunable refractive index matching medium for live imaging cells, tissues
522 and model organisms. *eLife* **6**, e27240 (2017).
523 16. Keller, P. J., Schmidt, A. D., Wittbrodt, J. & Stelzer, E. H. K. Reconstruction of zebrafish
524 early embryonic development by scanned light sheet microscopy. *Science* **322**, 1065–1069
525 (2008).
526 17. Olivier, N. *et al.* Cell Lineage Reconstruction of Early Zebrafish Embryos Using Label-Free
527 Nonlinear Microscopy. *Science* **329**, 967–971 (2010).
528 18. Berloco, M., Fanti, L., Breiling, A., Orlando, V. & Pimpinelli, S. The maternal effect gene,
529 abnormal oocyte (abo), of Drosophila melanogaster encodes a specific negative regulator of
530 histones. *Proc. Natl. Acad. Sci.* **98**, 12126–12131 (2001).
531 19. Gunjan, A. & Verreault, A. A Rad53 Kinase-Dependent Surveillance Mechanism that
532 Regulates Histone Protein Levels in S. cerevisiae. *Cell* **115**, 537–549 (2003).
533 20. Brown, D. T., Alexander, B. T. & Sittman, D. B. Differential effect of H1 variant
534 overexpression on cell cycle progression and gene expression. *Nucleic Acids Res.* **24**, 486–493
535 (1996).
536 21. Petridou, N. I., Corominas-Murtra, B., Heisenberg, C.-P. & Hannezo, E. Rigidity percolation
537 uncovers a structural basis for embryonic tissue phase transitions. *Cell* **184**, 1914-1928.e19
538 (2021).
539 22. Kuramoto, Y. *Chemical Oscillations, Waves, and Turbulence*. vol. 19 (Springer, Berlin,
540 Heidelberg, 1984).

541 23. Nolet, F. E. *et al.* Nuclei determine the spatial origin of mitotic waves. *eLife* **9**, e52868
542 (2020).
543 24. Murata-Hori, M., Tatsuka, M. & Wang, Y.-L. Probing the Dynamics and Functions of Aurora
544 B Kinase in Living Cells during Mitosis and Cytokinesis. *Mol. Biol. Cell* **13**, 1099–1108 (2002).
545 25. Kimmel, C. B. & Law, R. D. Cell lineage of zebrafish blastomeres: I. Cleavage pattern and
546 cytoplasmic bridges between cells. *Dev. Biol.* **108**, 78–85 (1985).
547 26. Conn, C. W., Lewellyn, A. L. & Maller, J. L. The DNA Damage Checkpoint in Embryonic
548 Cell Cycles Is Dependent on the DNA-to-Cytoplasmic Ratio. *Dev. Cell* **7**, 275–281 (2004).
549 27. Piñeros, L. *et al.* The nuclear-cytoplasmic ratio controls the cell cycle period in
550 compartmentalized frog egg extract. 2024.07.28.605512 Preprint at
551 https://doi.org/10.1101/2024.07.28.605512 (2024).
552 28. Minc, N., Burgess, D. & Chang, F. Influence of Cell Geometry on Division-Plane
553 Positioning. *Cell* **144**, 414–426 (2011).
554 29. Hertwig, O. *Das Problem der Befruchtung und der Isotropie des Eies: eine Theorie der*
555 *Vererbung*. (Verlag von Gustav Fischer, 1884).
556 30. Wold, S., Esbensen, K. & Geladi, P. Principal component analysis. *Chemom. Intell. Lab.*
557 *Syst.* **2**, 37–52 (1987).
558 31. Shamipour, S. *et al.* Bulk Actin Dynamics Drive Phase Segregation in Zebrafish Oocytes.
559 *Cell* **177**, 1463-1479.e18 (2019).
560 32. Danilova, N. *et al.* The role of the DNA damage response in zebrafish and cellular models
561 of Diamond Blackfan anemia. *Dis. Model. Mech.* **7**, 895–905 (2014).
562 33. Hadzhiev, Y. *et al.* A cell cycle-coordinated Polymerase II transcription compartment
563 encompasses gene expression before global genome activation. *Nat. Commun.* **10**, 691 (2019).
564 34. Giraldez, A. J. *et al.* Zebrafish MiR-430 Promotes Deadenylation and Clearance of Maternal
565 mRNAs. *Science* **312**, 75–79 (2006).

566 35. Heyn, P. *et al.* The Earliest Transcribed Zygotic Genes Are Short, Newly Evolved, and
567 Different across Species. *Cell Rep.* **6**, 285–292 (2014).
568 36. Summers, R. G. *et al.* A Stereometric Analysis of Karyokinesis, Cytokinesis and Cell
569 Arrangements during and following Fourth Cleavage Period in the Sea Urchin, Lytechinus
570 variegatus: (sea urchin embryo/cell division patterns/stereo imaging/3-D reconstruction). *Dev.*
571 *Growth Differ.* **35**, 41–57 (1993).
572 37. Logan, C. Y. & McClay, D. R. Lineages That Give Rise to Endoderm and Mesoderm in the
573 Sea Urchin Embryo. in *Cell Lineage and Fate Determination* 41–57 (Elsevier, 1999).
574 doi:10.1016/B978-012505255-9/50005-5.
575 38. Sulston, J. E., Schierenberg, E., White, J. G. & Thomson, J. N. The embryonic cell lineage
576 of the nematode Caenorhabditis elegans. *Dev. Biol.* **100**, 64–119 (1983).
577 39. Budke, H. *et al.* Assessment of cell proliferation in paraffin sections of normal bone marrow
578 by the monoclonal antibodies Ki-67 and PCNA. *Mod. Pathol.* **7**, 860–866 (1994).
579 40. Kelman, Z. PCNA: structure, functions and interactions. *Oncogene* **14**, 629–640 (1997).
580 41. Leung, A. Y. *et al.* Proliferating cell nuclear antigen (PCNA) as a proliferative marker during
581 embryonic and adult zebrafish hematopoiesis. *Histochem. Cell Biol.* **124**, 105–111 (2005).
582 42. Schindelin, J. *et al.* Fiji: an open-source platform for biological-image analysis. *Nat.*
583 *Methods* **9**, 676–682 (2012).
584 43. Arzt, M. *et al.* LABKIT: Labeling and Segmentation Toolkit for Big Image Data. *Front.*
585 *Comput. Sci.* **4**, (2022).
586 44. McKinney, W. Data Structures for Statistical Computing in Python. in 56–61 (Austin, Texas,
587 2010). doi:10.25080/Majora-92bf1922-00a.
588 45. Hunter, J. D. Matplotlib: A 2D Graphics Environment. *Comput. Sci. Eng.* **9**, 90–95 (2007).
589 46. Waskom, M. L. seaborn: statistical data visualization. *J. Open Source Softw.* **6**, 3021
590 (2021).

591 47. Stegmaier, J. *et al.* Real-Time Three-Dimensional Cell Segmentation in Large-Scale
592 Microscopy Data of Developing Embryos. *Dev. Cell* **36**, 225–240 (2016).
593 48. Bolte, S. & Cordelières, F. P. A guided tour into subcellular colocalization analysis in light
594 microscopy. *J. Microsc.* **224**, 213–232 (2006).
595 49. Tavano, S. *et al.* BMP-dependent patterning of ectoderm tissue material properties
596 modulates lateral mesendoderm cell migration during early zebrafish gastrulation.
597 2023.07.21.550024 Preprint at https://doi.org/10.1101/2023.07.21.550024 (2023).
598 50. Machado, S., Mercier, V. & Chiaruttini, N. LimeSeg: a coarse-grained lipid membrane
599 simulation for 3D image segmentation. *BMC Bioinformatics* **20**, 2 (2019).
600

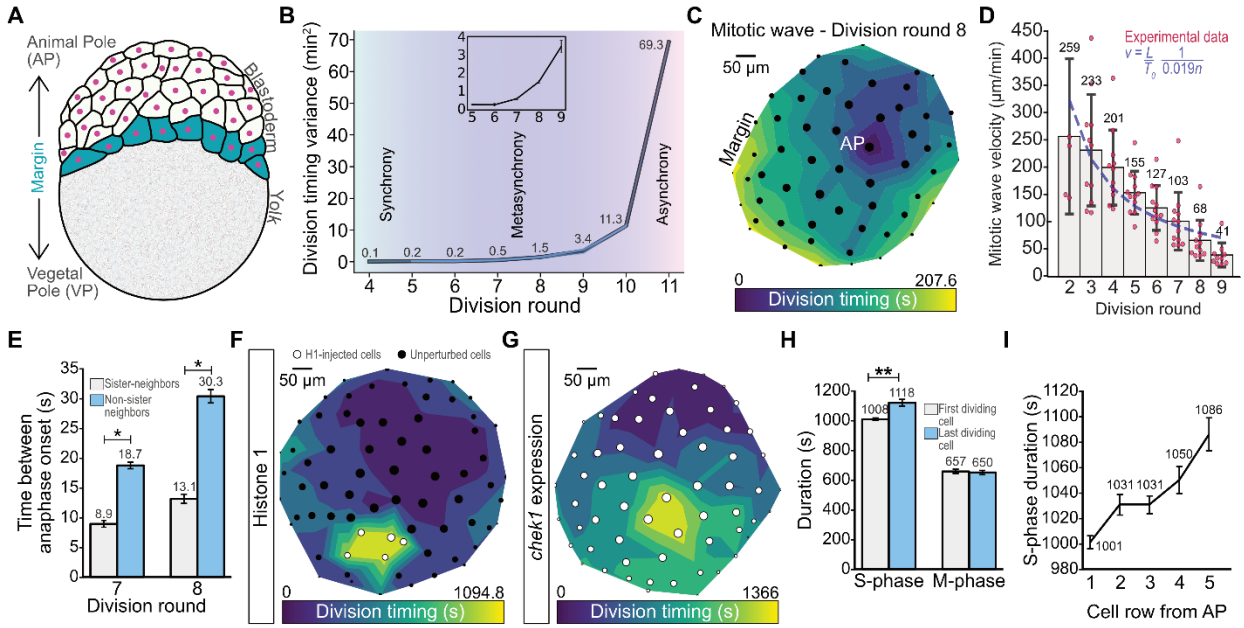

Fig. 1. Mitotic synchrony gradually decreases as the S-phase lengthens along the animal-margin axis. **(A)** Schematic representation of a zebrafish embryo at late cleavage stage. The blastoderm is positioned at the animal pole (AP) atop the yolk cell at the vegetal pole (VP). The last row of blastoderm cells (cyan) constitutes the margin. **(B)** Line plot of cell division timing variance in Tg(*actb2:rfp-pcna*) embryos for cleavage division rounds 4-11. Blue lines, individual embryos; black line, mean across 4 embryos. Inset shows variance for division rounds 5-9 **(C)** Contour plot of the radial mitotic wave across all surface cells at the 8th cleavage division round in a representative wild-type embryo. Each dot represents the position of a nucleus along the XY plane, and the size of the dot indicates its position along the Z-axis (AP-margin axis). Colors represent division timing for each nucleus. **(D)** Bar plot of mitotic wave velocities (mean ± SD), calculated by generating distance-time plots, for cleavage division rounds 2-9, with the red dots showing wave velocities for individual embryos. n=5-11 embryos. Blue dotted line: Curve described by the equation $v=(L/T_0).(1/0.019n)$, where L is the total AP-margin distance, T_0 is the cell cycle period at the AP, and n is the division round to represent the effect of a 1.9% period gradient along the AP-margin axis on mitotic wave speeds. **(E)** Bar plot of delay in anaphase onset between sister and non-sister neighbor cells (mean ± SEM) as a readout for cell division synchrony. n≥19 cell pairs; Student's t-test with $p<0.05$]. **(F,G)** Representative contour plots of mitotic waves at the 8th round of division in embryos injected with either 0.3pg Histone 1A protein into a single blastomere at the 32-cell stage (F) or 12pg *chek1* mRNA at the 1-cell stage. **(H)** Bar plot of M-phase and S-phase lengths (mean ± SD) at the 8th cleavage division round. n=8 embryos; Student's t-test with $p<0.01$]. **(I)** Line plot of S-phase duration (mean ± SEM) as a function of cell position relative to the AP. n≥4 embryos.

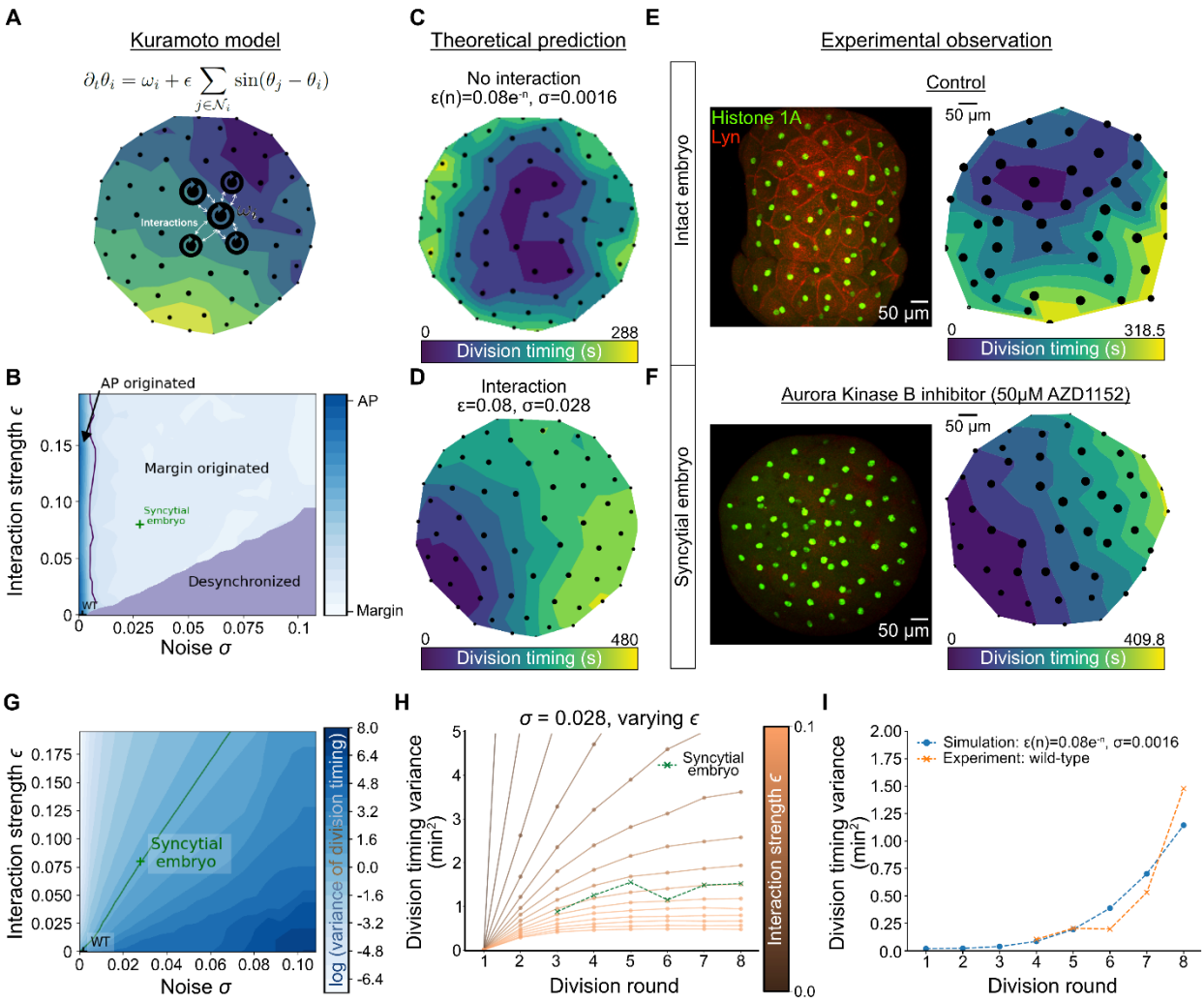

Fig. 2. Cell-cell coupling repositions the mitotic wave origin to the margin and prevents desynchronization. (A) Schematic representation of our adapted Kuramoto model and the equation describing the evolution of the phase of a cell cycle. Equation: θ_i represents the cell cycle phase of cell *i*, and N_i denotes its nearest neighboring cells, determined through Delaunay triangulation of the hemisphere. The coupling strength ϵ represents how strongly each cell influences its neighbors' timing. The intrinsic frequency ω_i represents how quickly cell *i* would progress through its cell cycle in isolation. Model: Each black dot represents a cell positioned on a hemispherical Fibonacci lattice. Dot size increases with height (*z*) to aid visualization in this top-down projection. Lines between dots (not shown) indicate coupled neighbors that can influence each other's cell cycle timing. **(B)** Phase diagram showing origin of the waves in ϵ-σ space. The boundary between AP originated and margin originated is thresholded at z=0.5 and the region of desynchronization corresponds to $\langle e^{i\theta_j} \rangle_j < 0.6$, where $\langle\rangle_j$ denotes averaging over all sites. **(C)** Contour plot of the radial mitotic wave across all surface cells at the 8th cleavage division round as predicted using the Kuramoto model of interacting oscillators, assuming an AP-margin period gradient of 1.9% and exponentially decaying cell-cell interaction strength (ϵ=0.08e^{-n}, σ=0.0016). **(D)** Contour plot of the mitotic wave across all surface cells at the 8th cleavage division round as predicted using the Kuramoto model of interacting oscillators, assuming an AP-margin period gradient of 1.9% and partial interaction between cells (ϵ=0.08, σ=0.028). **(E)** Left: Representative image of a 128-cell stage control Tg(*actb2:lyn-tdtomato*) embryo injected with 1pg Histone1A-Alexa Fluor 488 at the one-cell stage to show the presence of plasma membrane between individual nuclei. Right: Contour plot of the radial mitotic wave across all surface cells at the 8th cleavage division round observed in a control embryo, where nuclear divisions were visualized using either Histone1A-Alexa Fluor 488 injections or using Tg(*actb2:rfp-pcna*) embryos. n=7 embryos. **(F)** Left:

645 Representative image of a 128-cell stage Tg(*actb2:lyn-tdtomato*) embryo injected with 1pg Histone1A-Alexa
646 Fluor 488 at the one-cell stage and treated with 50μM AZD1152 to show the absence of plasma membrane
647 between individual nuclei. Right: Contour plot of the mitotic wave across all surface cells at the 8th cleavage
648 division round observed in a representative syncytial embryo, where nuclear divisions were visualized using
649 either Histone1A-Alexa Fluor 488 injections or using Tg(*actb2:rfp-pcna*) embryos. n=7 embryos. **(G)** Phase
650 diagram of the Kuramoto model in ε-σ space. The log of the variance of the division timings at the 8th round
651 is plotted. The green solid line indicates the contour line of the observed variance at the 8th round in syncytial
652 embryos. **(H)** Variances of division timings for each round for fixed noise value, σ=0.028 as ε varies. Green
653 dotted curve shows the variances measured in syncytial embryos. **(I)** Variances of division timings for each
654 round in wild-type embryos (orange) fitted with a curve described by exponentially decaying interaction
655 strength, $\varepsilon(n)=0.08e^{-n}$, and low noise, σ=0.0016 (blue).
656

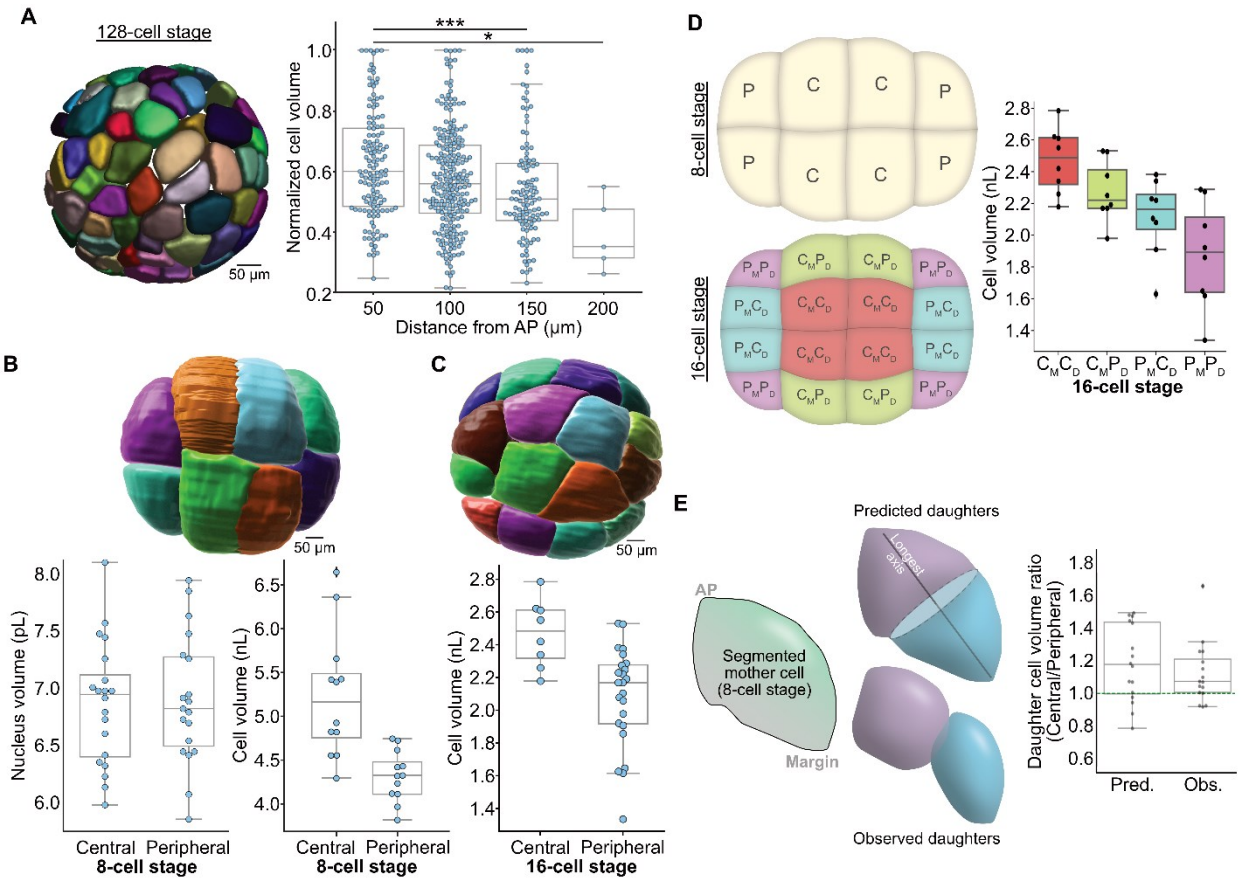

Fig. 3. Embryo geometry drives asymmetric cell divisions to generate a gradient of cell volumes in the early embryo. (A) Representative image of a 128-cell stage embryo (round 8) with surface cells segmented (left) and box-plot showing normalized cell volumes as a function of cell position with respect to the AP (right). Cell volumes were internally normalized by dividing each cell volume by the volume of the largest cell in the embryo. Each dot represents the data for an individual cell. (n=469 cells, 12 embryos). **(B)** Representative image of an 8-cell stage embryo (round 4) with surface cells segmented (top) and box-plot showing volumes of individual nuclei and cells based on their position relative to the AP (bottom). 'Central' cells are positioned at AP, whereas 'peripheral' cells are positioned away from the AP (n=20 central and 19 peripheral nuclei, 5 embryos; 12 central and 12 peripheral cells, 3 embryos). **(C)** Representative image of a 16-cell stage embryo (round 5) with surface cells segmented (top) and box-plot showing volumes of individual cells based on their position relative to the AP (bottom; n=8 central and 24 peripheral cells, 2 embryos). **(D)** Schematic showing the lineage relationship between cells at the 8-cell stage (top-left) and the 16-cell stage (bottom-left). At the 8-cell stage, cells marked 'C' are centrally positioned, and those marked 'P' are peripherally positioned. At the 16-cell stage, cells are labelled to indicate both their positions (C_D, centrally; P_D, peripherally) and the identities of their mother cells (C_M, centrally positioned mother cell; P_M, peripherally positioned mother cell). Box plot showing the distribution of cell volumes at the 16-cell stage based on each cell's position and lineage identity (right) (n=8 cells for each category, 2 embryos). **(E)** Schematic showing the pipeline for predicting daughter cell volumes at the 16-cell stage (left). Each segmented cell surface from the 8-cell stage was used to identify the longest cell axis, which was then bisected to obtain daughter cells at the 16-cell stage. Violin plot showing a comparison between the ratios of volumes of the central and peripheral daughter cells obtained from each cell division, respectively, either predicted (Pred.) or experimentally measured (Obs.) (right; n=16 cell pairs, 2 embryos).

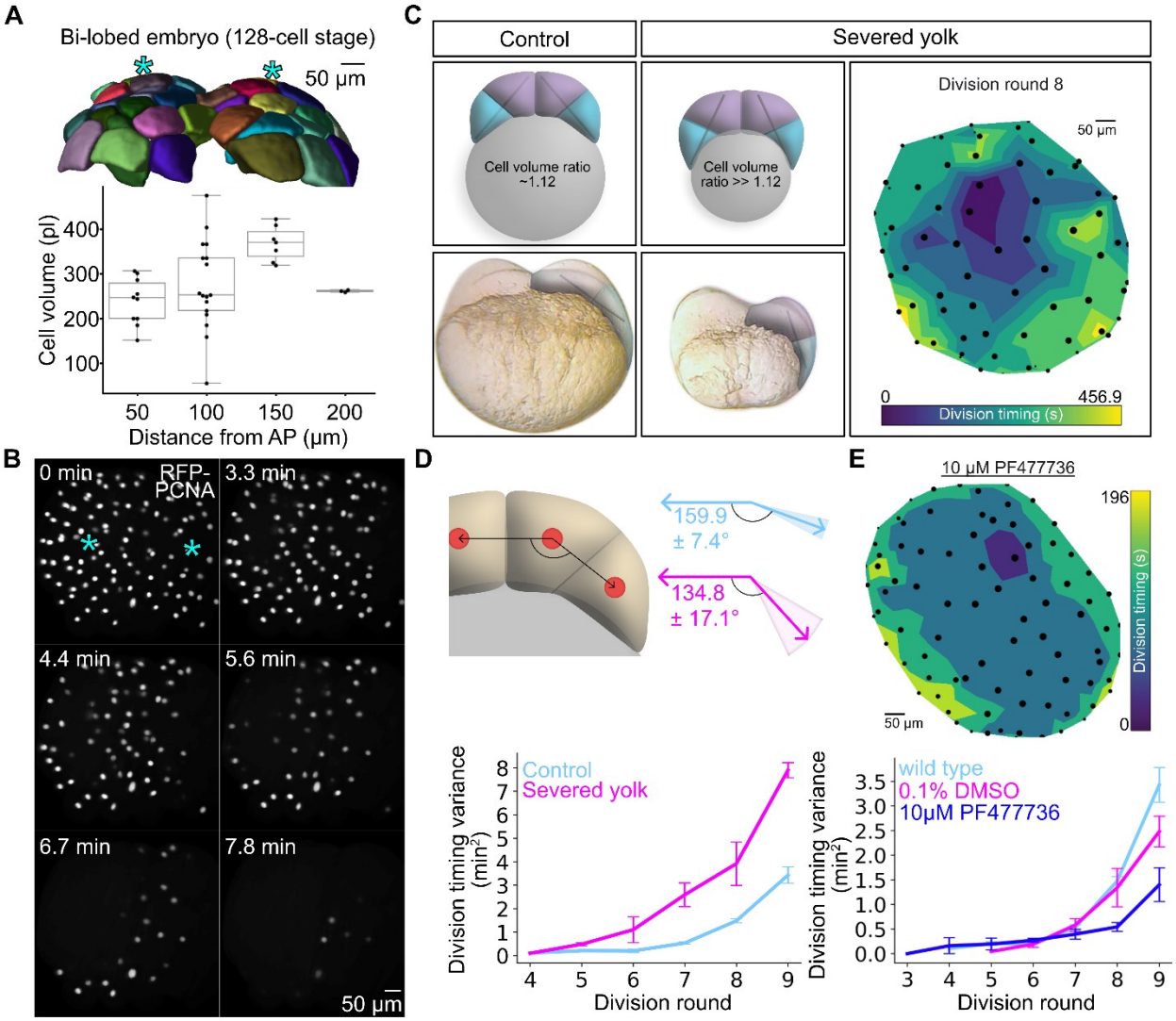

Fig. 4. AP-margin cell volume gradient increases cell cycle metasynchrony in a Chek1-dependent manner. (A) Representative image of a 128-cell stage (round 8) bi-lobed embryo with surface cells segmented (top) and box-plot showing normalized cell volumes as a function of cell position with respect to the AP (right) for this embryo. Cyan asterisks mark the ectopic animal poles in the bi-lobed embryo. **(B)** Montage of images showing the propagation of mitotic waves in a representative bi-lobed Tg(*actb2:rfp-pcna*) embryo at the 8th division round. Cyan asterisks mark the ectopic animal poles in the bi-lobed embryo (n=5 embryos). **(C)** Schematic representations (top-left) and representative images (bottom-left) of a control embryo and an embryo where the yolk has been severed at the two-cell stage to increase the curvature of the blastoderm-to-yolk cell interface. Lines inside the cells indicate the longest cell axis along which the divisions (division round 3) are expected to occur. Cells marked in magenta and cyan represent the resulting central and marginal daughter cells, respectively. Contour plot (right) shows mitotic wave propagation in the 8th division round of a yolk-severed embryo (AP-view). **(D)** Schematic representation (top) of the decreased angle of cell divisions in the 4th division round in yolk-severed embryos due to an increased curvature of the blastoderm-to-yolk cell interface compared to corresponding control embryos (angles are mean ± SD; n>10 cells). Line plot (bottom) showing the variance in cell division timings in control and yolk-severed embryos (mean ± SD; n=4 embryos). **(E)** Representative contour plot (top) showing mitotic wave propagation in a Chek1 inhibitor (PF477736)-treated embryo in division round 8 (AP-view). Line plot (bottom) showing the variance in cell division timings in control and PF477736-treated embryos (mean ± SD; n=4 embryos).

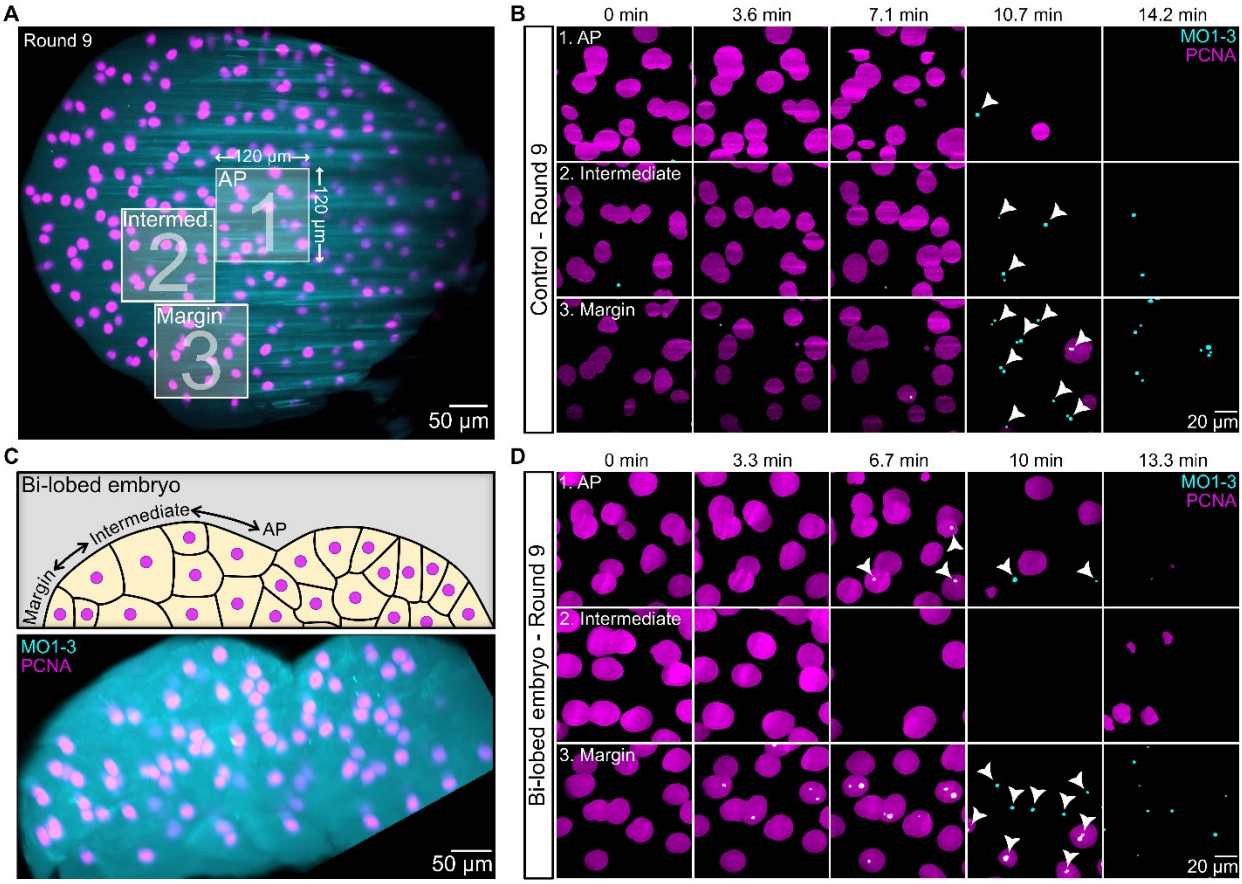

Fig. 5. Zygotic transcription is initiated in a patterned manner along the AP-margin axis. (A) Representative maximum intensity projection image showing an animal pole-view of a control Tg(*actb2:rfp-pcna)* embryo injected with MO1-3-Fluorescein in the 9th division round. Cyan, MO1-3-Fluorescein; magenta, nuclei (PCNA). The three insets, each 120 µm X 120 µm in size, demarcate the regions (1, animal pole; 2, intermediate region; 3, margin) whose higher-magnification images are shown in (B) and (D). **(B)** Zoomed-in views of the insets shown in A. Cyan dots represent nascent *mi430* transcripts detected by MO1-3-Fluorescein (n=4 embryos). **(C)** A schematic (top) and a representative orthogonal maximum intensity projection image (bottom) of a bi-lobed Tg(*actb2:rfp-pcna)* embryo injected with MO1-3-Fluorescein embryo in the 9th division round. Cyan, MO1-3-Fluorescein; magenta, nuclei (PCNA). **(D)** Zoomed-in views of the equivalent regions (1, animal pole; 2, intermediate region; 3, margin) demarcated in (A) for a bi-lobed embryo in the 9th division round. Cyan dots represent nascent *mi430* transcripts (n=3 embryos).

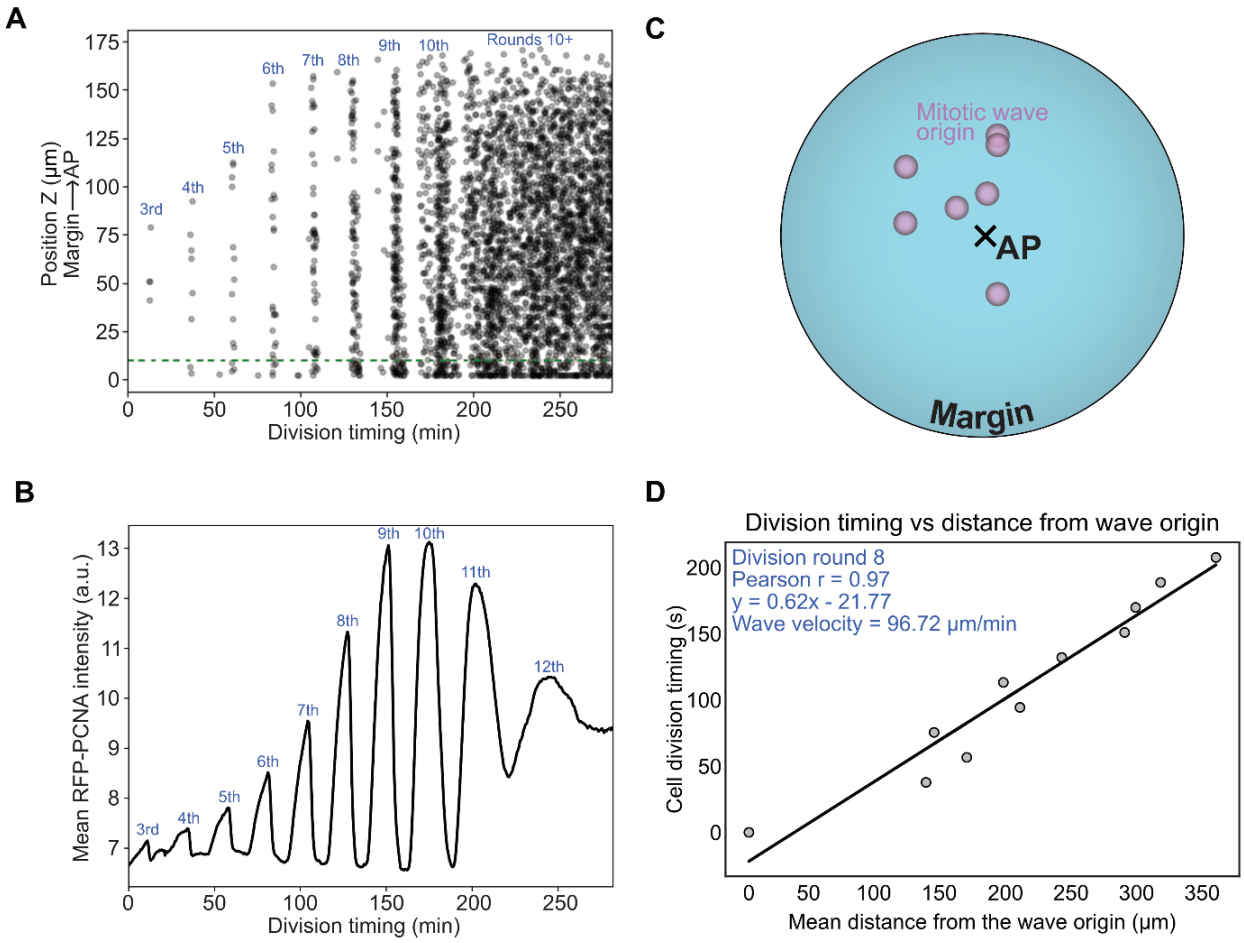

Fig. S1. Cells cycle periodically, and their division timings correlate linearly with their distance from the wave origin.

(A) Scatter plot of division timing for individual cells starting at cleavage division round 3 (x-axis) relative to their position along the animal-margin axis (y-axis) for one representative wild-type embryo. The green dotted line outlines cells located at a distance of <10 µm from the bottom of the image stack that could not be reliably tracked. **(B)** Mean RFP-PCNA intensity, as a marker for mitosis onset, as a function of time. Mean PCNA intensity increases during the S-phase, peaks just before the S-M transition, and declines in the M-phase. Thus, a narrow peak indicates greater synchrony and vice versa. **(C)** Representative scheme showing the position of the mitotic wave origin in division round 8 (n=7 embryos). **(D)** Representative plot of cleavage division timing as a function of cell distance from the mitotic wave origin in cleavage division round 8 from a wild-type embryo. Cells undergoing the S-M transition were binned together.

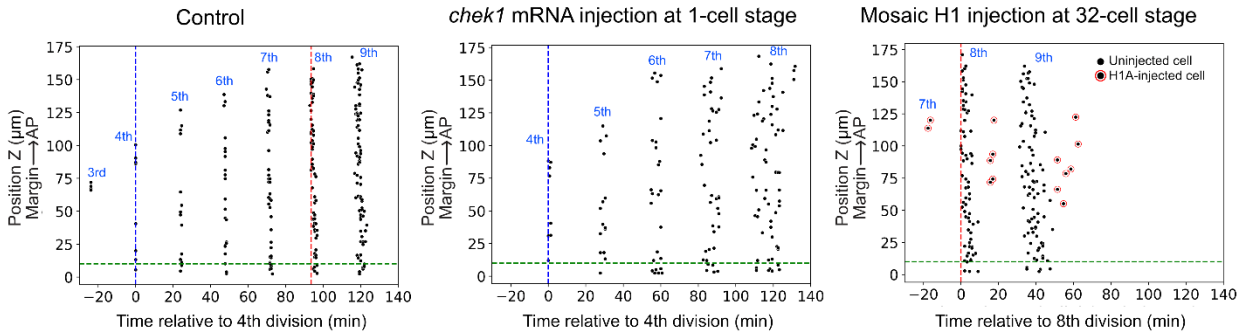

Fig. S2. Desynchronized cell cycles do not resynchronize during cleavages.

Representative scatter plots of the division timing for individual surface cells relative to their position along the animal-margin axis in control embryos (left), and embryos injected with either 12pg *chek1* mRNA at the 1-cell stage (middle) or 0.3pg Histone1A protein at the 32-cell stage (right). Blue and red dotted lines demarcate the onset of the 4th and 8th cleavage divisions, respectively. Green dotted line outlines cells located at a distance of <10 µm from the bottom of the image stack that could not be reliably tracked.

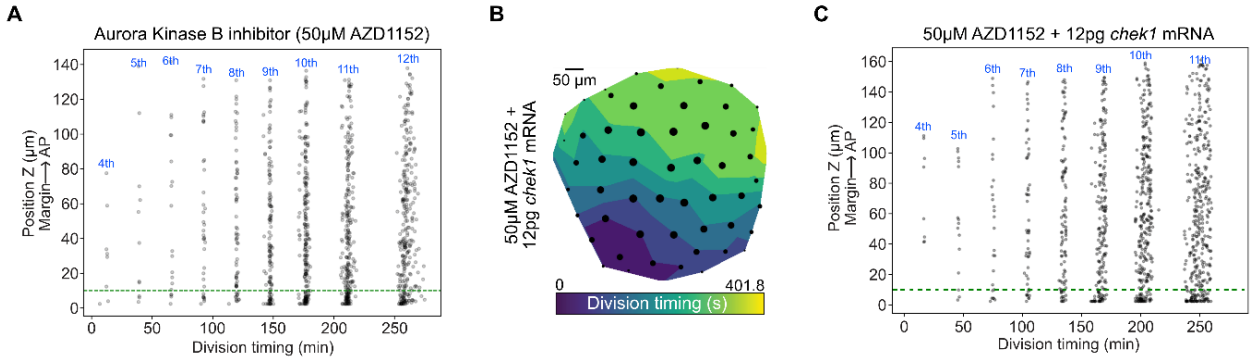

Fig. S3. Mitotic wave originates at the margin and persists after division round 10 in syncytial embryos

(A) Representative scatter plot of the division timings for individual cells relative to their position along the animal-margin axis in a syncytial Tg(*actb2:rfp-pcna*) embryo (n=7 embryos). **(B)** Contour plot of the mitotic wave across all surface cells at the 8th round of cleavage division round in syncytialized Tg(*actb2:rfp-pcna*) embryos injected with 12pg *chek1* mRNA at the one-cell stage, and **(C)** a scatter plot of division timings relative to position along the AP-margin axis for a representative syncytial embryo injected with 12pg *chek1* mRNA (n=4 embryos).

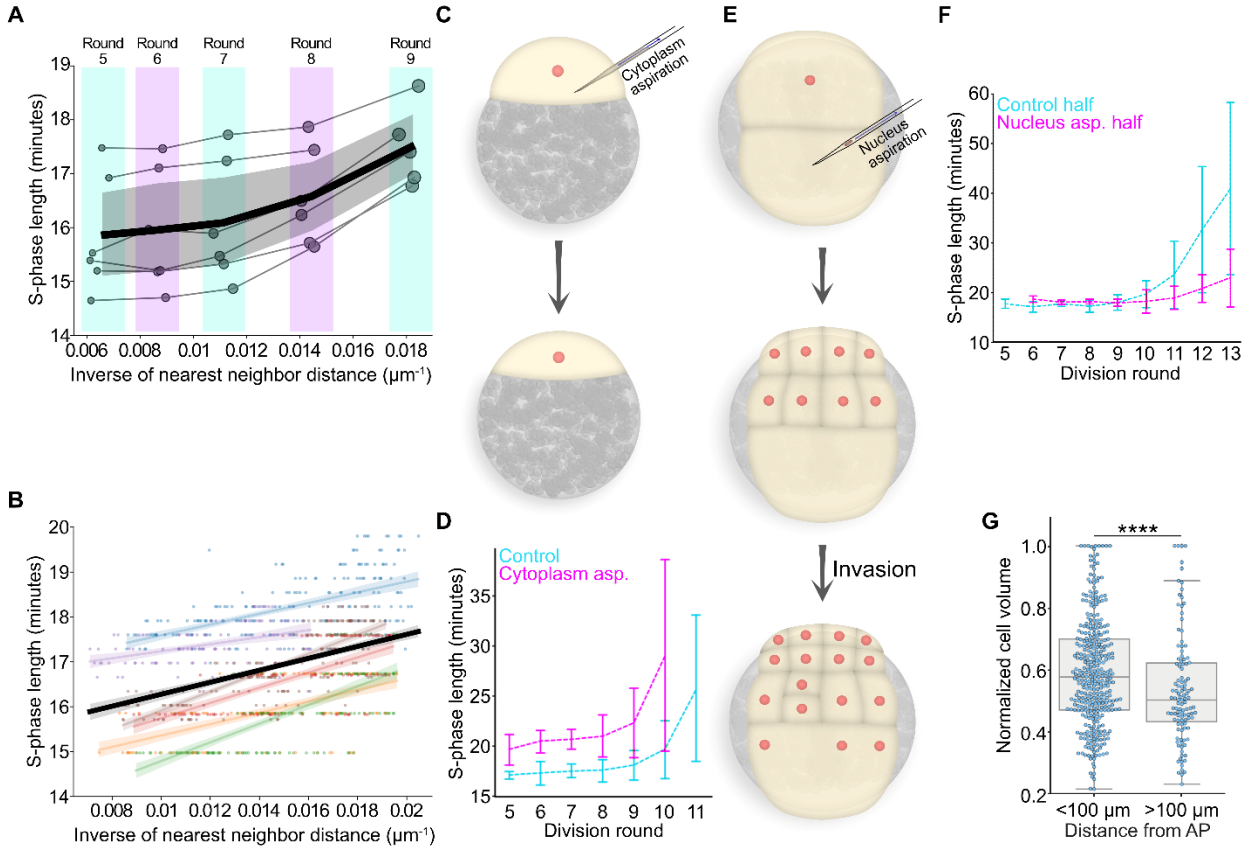

Fig. S4. Cell volume regulates S-phase length

(A) Line plots showing mean S-phase lengths in individual (thin, grey lines) and across (thick, black line, mean ± 95% CI) embryos as a function of the inverse of the mean nearest neighbor distance (mean of 3) in the metasynchronous cell cycle stages. Division rounds are indicated by the size of the dots (smallest: division round 5, largest: division round 9 (n=6 embryos) and also indicated at the top. **(B)** Linear regression plots showing the relationship between the inverse of the nearest neighbor distance (mean of 3) for each cell and the length of its S-phase. Dots represent single cells, whereas the lines show the best-fit linear curve for the data. Each color represents the data for a unique embryo. The thick, black line shows a summary best-fit for the data of all cells across all embryos. For each embryo, cells only within the 5th-95th percentile of their nearest neighbor distances and S-phase length were considered for the analysis, which minimizes erroneous measurements at the extremes but also underestimates the relationship (n=6 embryos, 964 cells). **(C)** Schematic representation of the experiment where a fraction of the cytoplasm was aspirated from the blastodisc within approximately 10 minutes before the first cell division to increase the nucleocytoplasmic ratio. **(D)** Representative line plot showing S-phase length in each division round in control embryos and embryos from which cytoplasm was aspirated (mean ± SD, n=3 embryos). **(E)** Schematic representation of the experiment where one of the nuclei at the two-cell stage was aspirated to decrease the nucleocytoplasmic ratio in the aspirated half of the embryo (top). Only the nucleated, control half initially develops (i.e. shows mitotic cycles) (middle) until nuclei from this half invade the enucleated half (bottom), which then begins to develop with a smaller nucleocytoplasmic ratio. **(F)** Representative line plot showing S-phase length in each

division round in the control and enucleated halves of the embryo depicted in (E) (mean ± SD, n=3 embryos). **(G)** Box-plot showing normalized cell volumes as a function of cell position with respect to the AP. Cell volumes were internally normalized by dividing each cell volume by the volume of the largest cell in the embryo. Each dot represents the data for an individual cell. Data is the same as in Fig. 3A, but the cells here have been classified into only two bins (n=469 cells, 12 embryos; Student's t-test, $p<0.001$).

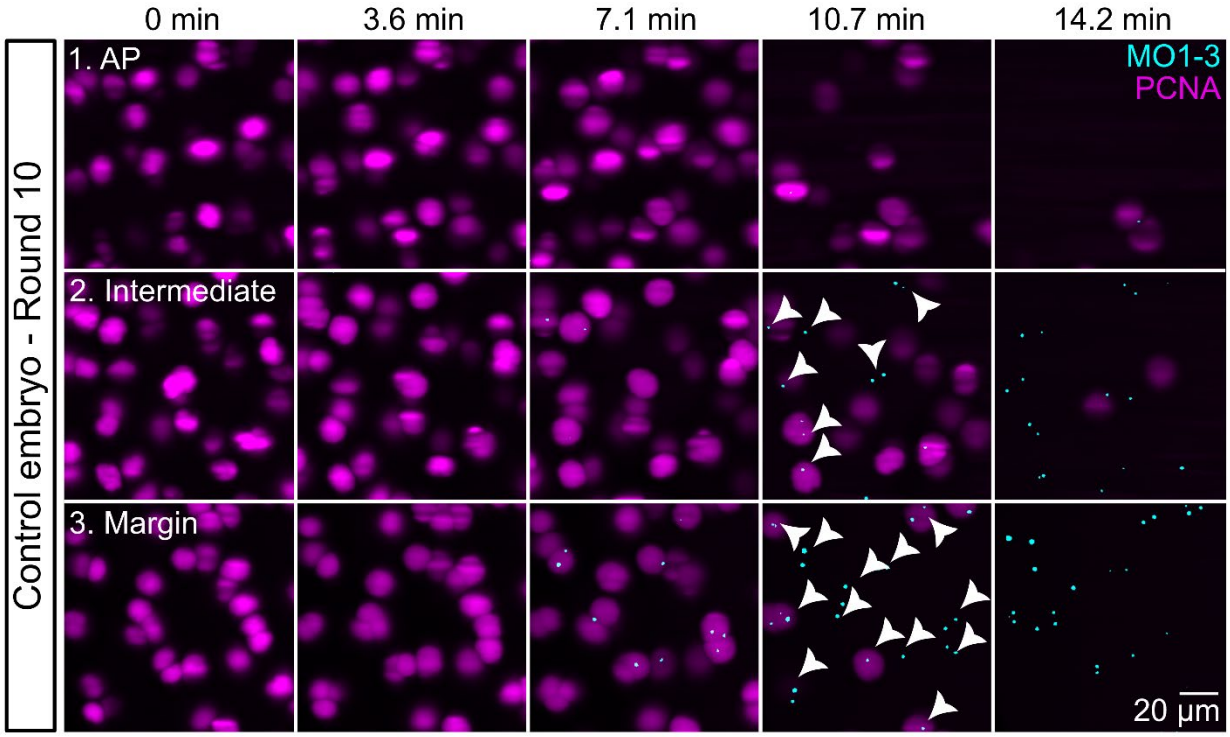

Fig. S5. Zygotic transcription is initiated in a patterned manner along the AP-margin axis

Zoomed-in views of the insets (1, animal pole; 2, intermediate region; 3, margin) shown in Fig. 5A for a control Tg(*actb2:rfp-pcna)* embryo injected with MO1-3-Fluorescein in the 10th division round. Cyan, MO1-3-Fluorescein (nascent *mi430* transcripts); magenta, nuclei (PCNA). Each inset represents an area of 120 µm X 120 µm in size.

Movie S1.
Animal pole (AP)-view of the cell cycle progression beginning from division round 3 in a Tg(*actb2:rfp-pcna*) embryo. Temporal resolution: 38.7 seconds/frame.

Movie S2.
AP-view of the cell cycle progression beginning from division round 7 in a Tg(*actb2:rfp-pcna*) embryo with a mosaic injection of 0.3pg Histone 1-Alexa Flour 488 at the 32-cell stage. The highlighted region indicates the position of the (daughters of the) injected cells. Red: PCNA, Green: Histone 1. Temporal resolution: 39.1 seconds/frame.

Movie S3.
AP-view of the cell cycle progression beginning from division round 4 in a Tg(*actb2:rfp-pcna*) embryo injected with 12pg *chek1* mRNA at the one-cell stage. Temporal resolution: 37.9 seconds/frame.

Movie S4.
AP-view of the nuclear cycling beginning from division round 4 in a Tg(*actb2:rfp-pcna*) embryo syncytialized by inhibiting Aurkb activity through 50µM AZD1152-treatment at the one-cell stage. Temporal resolution: 38.1 seconds/frame.

Movie S5.
AP-view of the nuclear cycling beginning from division round 3 in a syncytialized Tg(*actb2:rfp-pcna*) embryo injected with 12pg *chek1* mRNA at the one-cell stage. Temporal resolution: 57.4 seconds/frame.

Movie S6.
AP-view of the cell cycle progression beginning from division round 4 in a Tg(*actb2:rfp-pcna*) embryo from which one nucleus at the two-cell stage was aspirated. (Top: Control half, Bottom: Nucleus aspiration half). Temporal resolution: 71.8 seconds/frame.

Movie S7.
AP-view of the cell cycle progression beginning from division round 4 in a bi-lobed Tg(*actb2:rfp-pcna*) embryo. Temporal resolution: 66.7 seconds/frame.

Movie S8.
AP-view of the cell cycle progression beginning from division round 5 in a Tg(*actb2:rfp-pcna*) embryo with the yolk-blastoderm curvature increased through a partial severing of the yolk at the two-cell stage. Temporal resolution: 65.3 seconds/frame.

Movie S9.
AP-view of the cell cycle progression beginning from division round 3 in a Tg(*actb2:rfp-pcna*) embryo treated with 10µM PF477736 to inhibit Chek1 activity. Temporal resolution: 65.9 seconds/frame.

Movie S10.
AP-view of the cell cycle progression and *mirR430* pri-mRNA beginning from division round 8 in a control Tg(*actb2:rfp-pcna*) embryo injected with MO1-3-Fluorescein at the one-cell stage. Magenta: PCNA, Cyan: MO1-3. Temporal resolution: 53.4 seconds/frame.

Movie S11.
AP-view of the cell cycle progression and *mirR430* pri-mRNA beginning from division round 8 in a bi-lobed Tg(*actb2:rfp-pcna*) embryo injected with MO1-3-Fluorescein at the one-cell stage. Magenta: PCNA, Cyan: MO1-3. Temporal resolution: 66.7 seconds/frame.